

Geometry-Complete Perceptron Networks for 3D Molecular Graphs

Alex Morehead^{1*} and Jianlin Cheng^{1*}

^{1*}Electrical Engineering & Computer Science, University of
Missouri-Columbia, W1024 Lafferre Hall, Columbia, 65211, Missouri,
United States of America.

*Corresponding author(s). E-mail(s): acmwhb@missouri.edu;
chengji@missouri.edu;

Abstract

The field of geometric deep learning has had a profound impact on the development of innovative and powerful graph neural network architectures. Disciplines such as computer vision and computational biology have benefited significantly from such methodological advances, which has led to breakthroughs in scientific domains such as protein structure prediction and design. In this work, we introduce GCPNET, a new geometry-complete, $SE(3)$ -equivariant graph neural network designed for 3D molecular graph representation learning. Rigorous experiments across four distinct geometric tasks demonstrate that GCPNET’s predictions (1) for protein-ligand binding affinity achieve a statistically significant correlation of 0.608, more than 5% greater than current state-of-the-art methods; (2) for protein structure ranking achieve statistically significant target-local and dataset-global correlations of 0.616 and 0.871, respectively; (3) for Newtonian many-body systems modeling achieve a task-averaged mean squared error less than 0.01, more than 15% better than current methods; and (4) for molecular chirality recognition achieve a state-of-the-art prediction accuracy of 98.7%, better than any other machine learning method to date. The source code, data, and instructions to train new models or reproduce our results are freely available at <https://github.com/BioinfoMachineLearning/GCPNet>.

Keywords: Geometric deep learning, equivariance, graph neural networks, computational biology, molecules, proteins

success cases in using deep neural networks to faithfully model geometric data in the form of 3D graphs and manifolds [12, 13].

Previous works in geometric deep learning [14] have explored the use of neural networks for modeling physical systems [15–17]. Some of the earliest neural networks applied to physical systems include convolutional networks (CNNs) [18–21], graph neural networks (GNNs) [22–25], and point cloud neural networks [26–28]. Likewise, recurrent neural networks (RNNs) have been used to classify sequential real-world data such as speech activity [29, 30] and have been adopted as case studies for how to develop next-generation wave-based electronics hardware [31].

In scientific domains such as computational biology and chemistry, graphs are often used to represent the 3D structures of molecules [32, 33], chemical compounds [34], and even large biomolecules such as proteins [35, 36]. Graphs have even been used in fields such as computational physics to model complex particle physics simulations [37] as well as in real-world traffic systems to predict travel times and delays [38]. Underlying many of these successful examples of graph representations are GNNs, a class of machine learning algorithms specialized in processing irregularly-structured input data such as graphs. Careful applications of graph neural networks in scientific domains have considered the physical symmetries present in many scientific data such as molecular state symmetries [39] or physical dynamics constraints [40] and have leveraged such symmetries to design new attention-based neural network architectures [41, 42].

Throughout their development, geometric deep learning methods have expanded to incorporate within them equivariance to various geometric symmetry groups to enhance their generalization capabilities and adversarial robustness. Methods such as group-equivariant CNNs [43], Tensor Field Networks [44], SE(3)-Transformers [45], and equivariant GNNs [45–55] have paved the way for the development of future deep learning models that respect physical symmetries present in 3D data (e.g., rotation equivariance with respect to input data symmetries). Concurrently to these efforts, self-supervised learning methods have begun to facilitate automatic detection and enforcement of the symmetries present in input data within the network’s representations for such inputs [56]. Nonetheless, deciding how to optimize self-supervised learning algorithms for one’s desired level of equivariance has proven to be a challenging task [57].

In total, in this work, we make connections between geometric graph neural networks, equivariance, and geometric information-completeness guarantees that provide one with a rich foundation on which to build new graph neural network architectures. In particular, we introduce a new graph neural network model, GCPNET, that is equivariant to the group of 3D rotations and translations (i.e., SE(3), the special Euclidean group) and guarantees geometric information completeness following graph message-passing on 3D point clouds. We demonstrate its expressiveness and flexibility for modeling physical systems through rigorous experiments for distinct molecular-geometric tasks. In detail, we provide the following contributions:

- In contrast to prior geometric networks for molecules that are insensitive to their chemical chirality, cannot detect global physical forces acting upon each atom, or

do not directly learn geometric features, we present the first geometric graph neural network architecture with the following desirable properties for learning from 3D molecules: (1) the ability to directly predict translation and rotation-invariant scalar properties and rotation-equivariant vector-valued quantities for nodes and edges, respectively; (2) a rotation and translation-equivariant method for iteratively updating node positions in 3D space; (3) sensitivity to molecular chirality; and (4) a means by which to learn from and account for the global forces acting upon the atoms within its inputs.

- We establish new state-of-the-art results for four distinct molecular-geometric representation learning tasks - molecular chirality recognition, protein-ligand binding affinity prediction, protein structure ranking, and Newtonian many-body-systems modeling - where model predictions vary from analyzing individual nodes to summarizing entire graph inputs. GCPNET’s performance for these tasks is statistically significant and surpasses that of previous state-of-the-art machine learning methods for 3D molecules.

2 Results

In this work, we consider four distinct modeling tasks comprised of seven datasets in total, where implementation details are discussed in Appendix C. We note that additional experiments are included in Appendix B for interested readers.

Assessing model sensitivity to molecular chirality. Molecular chirality is an essential geometric property of 3D molecules for models to consider when making predictions for downstream tasks. Simply put, this property describes the "handedness" of 3D molecules, in that, certain molecules cannot be geometrically superimposed upon a mirror reflection of themselves using only 3D rotation and translation operations. This subsequently poses a key challenge for machine learning models: Can such predictive models effectively sensitize their predictions to the effects of molecular chirality such that, under 3D reflections, their molecular feature representations change accordingly? To answer this question using modern machine learning methods, we adopt the rectus/sinister (RS) 3D molecular dataset of [58] to evaluate the ability of state-of-the-art machine learning methods to distinguish between right-handed and left-handed versions of a 3D molecule. In addition, we carefully follow their experimental setup including dataset splitting and evaluation criteria, where we evaluate each method’s classification accuracy in distinguishing between right and left-handed versions of a molecule. Baseline methods for this task include state-of-the-art invariant neural networks (INNs) and equivariant neural networks (ENNs), where we list each method’s latest results for this task as reported in [59].

Contribution of frame embeddings for chirality sensitivity. Table 1 shows that GCPNET is more accurately able to detect the effects of molecular chirality compared to all other baseline methods, even without performing any hyperparameter tuning. In particular, GCPNET outperforms ChIRo [58], a GNN specifically designed to detect different forms of chirality in 3D molecules. Moreover, when we ablate GCPNET’s embeddings of local geometric frames, we find that this E(3)-equivariant (i.e., 3D rotation *and* reflection-equivariant) version of GCPNET is no longer able to solve

Table 1: Comparison of GCPNET with baseline methods for the RS task. The results are averaged over three independent runs. The top-1 (best) results for this task are in **bold**, and the second-best results are underlined.

Type	Method	R/S Accuracy (%) \uparrow
INN	ChIRo [2023]	<u>98.5</u>
	SchNet [2023]	54.4
	DimeNet++ [2023]	65.7
	SphereNet [2023]	98.2
ENN	EGNN [2023]	50.4
	SEGNN [2023]	83.4
Ours	GCPNET w/o Frames	50.2 \pm 0.6
	GCPNET	98.7 \pm 0.1

this important molecular recognition task, resulting in prediction accuracies at parity with random guessing. These two previous observations highlight that (1) GCPNET’s local frame embeddings are critical components of the model’s sensitivity to molecular chirality and that, (2) using such frame embeddings, GCPNET can flexibly learn representations of 3D molecules that are more predictive of chemical chirality compared to hand-crafted methods for such tasks.

Evaluating predictions of protein-ligand binding affinity. Protein-ligand binding affinity (LBA) prediction challenges methods to estimate the binding affinity of a protein-ligand complex as a single scalar value [60]. Accurately estimating such values in a matter of seconds using a machine learning model can provide invaluable and timely information in the typical drug discovery pipeline [73]. The corresponding dataset for this SE(3)-invariant task is derived from the ATOM3D dataset [60] and is comprised of 4,463 nonredundant protein-ligand complexes, where cross-validation splits are derived using a strict 30% sequence identity cutoff. Results are reported in terms of the root mean squared error (RMSE), Pearson’s correlation (p), and Spearman’s correlation (Sp) between a method’s predictions on the test dataset and the corresponding ground-truth binding affinity values represented as $pK = -\log_{10}(K)$, where K is the binding affinity measured in Molar units. Baseline comparison methods for this task include a variety of state-of-the-art CNNs, recurrent neural networks (RNNs), GNNs, and ENNs.

The results shown in Table 2 reveal that, in operating on atom-level protein-ligand graph representations, GCPNET achieves the best performance for predicting protein-ligand binding affinity by a significant margin, notably improving performance across all metrics by 7% on average. Here, to the best of our knowledge, GCPNET is also the first method capable of achieving Pearson and Spearman binding affinity correlations greater than 0.6 on the PDBBind dataset [74] when employing a strict 30% sequence

Table 2: Comparison of GCPNET with baseline methods for the LBA task. The results are averaged over three independent runs. The top-1 (best) results for this task are in **bold**, and the second-best results are underlined.

Type	Method	RMSE ↓	p ↑	Sp ↑
CNN	3DCNN [2020]	1.416 ± 0.021	0.550	0.553
	DeepDTA [2018]	1.866 ± 0.080	0.472	0.471
	DeepAffinity [2019]	1.893 ± 0.650	0.415	0.426
RNN	Bepler and Berger [2019]	1.985 ± 0.006	0.165	0.152
	TAPE [2019]	1.890 ± 0.035	0.338	0.286
	ProtTrans [2021]	1.544 ± 0.015	0.438	0.434
GNN	GCN [2020]	1.601 ± 0.048	0.545	0.533
	DGAT [2021]	1.719 ± 0.047	0.464	0.472
	DGIN [2021]	1.765 ± 0.076	0.426	0.432
	DGAT-GCN [2021]	1.550 ± 0.017	0.498	0.496
	MaSIF [2020]	1.484 ± 0.018	0.467	0.455
	IEConv [2021]	1.554 ± 0.016	0.414	0.428
	Holoprot-Full Surface [2021]	1.464 ± 0.006	0.509	0.500
	Holoprot-Superpixel [2021]	1.491 ± 0.004	0.491	0.482
	ProNet-Amino-Acid [2023]	1.455 ± 0.009	0.536	0.526
	ProNet-Backbone [2023]	1.458 ± 0.003	0.546	0.550
	ProNet-All-Atom [2023]	1.463 ± 0.001	0.551	0.551
	GeoSSL-DDM [2023]	1.451 ± 0.030	<u>0.577</u>	<u>0.572</u>
	ENN	Cormorant [2019]	1.568 ± 0.012	0.389
PaiNN [2021]		1.698 ± 0.050	0.366	0.358
ET [2022]		1.490 ± 0.019	0.564	0.532
GVP [2021]		1.594 ± 0.073	0.434	0.432
GBP [2022]		<u>1.405 ± 0.009</u>	0.561	0.557
Ours	GCPNET w/o Frames	1.485 ± 0.015	0.521	0.504
	GCPNET w/o RESGCP	1.514 ± 0.008	0.471	0.468
	GCPNET w/o Scalars	1.685 ± 0.000	0.050	0.000
	GCPNET w/o Vectors	1.727 ± 0.005	0.270	0.304
	GCPNET	1.352 ± 0.003	0.608	0.607

identity cutoff. Moreover, we find that these correlations are highly statistically significant (i.e., Pearson’s p-value of $2e - 50$, Spearman’s p-value of $2e - 49$, and Kendall’s tau correlation of 0.432 with a p-value of $3e - 45$).

Ablating network components reveals impact of model design. Denoted as ”GCPNET w/o ...” in Table 2, our ablation studies with GCPNET for the LBA task demonstrate the contribution of each component in its model design. In particular, our proposed local frame embeddings improve GCPNET’s performance by more than 15% across all metrics (GCPNET w/o Frames), where we hypothesize these performance improvements come from using these frame embeddings to enhance the model’s sensitivity to molecular chirality. Similarly, our proposed residual GCP module (i.e., RESGCP) improves GCPNET’s performance by 23% on average.

Table 3: Comparison of GCPNET with baseline methods for the PSR task. Local metrics are averaged across target-aggregated metrics. The best results for this task are in **bold**, and the second-best results are underlined. N/A denotes a metric that could not be computed.

Method	Local			Global		
	$p \uparrow$	$Sp \uparrow$	$K \uparrow$	$p \uparrow$	$Sp \uparrow$	$K \uparrow$
3DCNN [2020]	0.557	0.431	0.308	0.780	0.789	0.592
GCN [2020]	0.500	0.411	0.289	0.747	0.750	0.547
ProQ3D [2017]	0.444	0.432	0.304	0.796	0.772	0.594
VoroMQA [2017]	0.412	0.419	0.291	0.688	0.651	0.505
RWplus [2010]	0.192	0.167	0.137	0.033	0.056	0.011
SBROD [2019]	0.431	0.413	0.291	0.551	0.569	0.393
Ornate [2019]	0.393	0.371	0.256	0.625	0.669	0.481
DimeNet [2020]	0.302	0.351	0.285	0.614	0.625	0.431
GraphQA [2021]	0.357	0.379	0.251	0.821	0.820	0.618
PaiNN [2021]	0.518	0.444	0.315	0.773	0.813	0.611
ET [2021]	0.564	0.466	0.330	0.813	0.814	0.611
GVP [2021]	0.581	0.462	0.331	0.805	0.811	0.616
GBP [2022]	<u>0.612</u>	<u>0.517</u>	<u>0.372</u>	<u>0.856</u>	<u>0.853</u>	<u>0.656</u>
GCPNET w/o Frames	0.588	0.512	0.367	0.854	0.851	0.657
GCPNET w/o RESGCP	0.576	0.509	0.365	0.852	0.847	0.648
GCPNET w/o Scalars	N/A	N/A	N/A	N/A	N/A	N/A
GCPNET w/o Vectors	0.571	0.497	0.356	0.802	0.804	0.608
GCPNET	0.616	0.534	0.385	0.871	0.869	0.676

Specifically of interest is the observation that independent removal of scalar and vector-valued features within GCPNET appears to severely decrease GCPNET’s performance for LBA prediction. Notably, removing the model’s access to scalar-valued features degrades performance by 70% on average, while not allowing the model to access vector-valued features reduces performance by 42% on average. One possible explanation for these observations is that both types of feature representations the baseline GCPNET model learns (i.e., scalars and vectors) are useful for understanding protein-ligand interactions. In addition, our ablation results in Table 2 suggest that our proposed frame embeddings and RESGCP module are complementary to these scalar and vector-valued features in the context of predicting the binding affinity of a protein-ligand complex.

Evaluating ranking predictions for protein structure decoys. Protein structure ranking (PSR) requires methods to predict the overall quality of a 3D protein structure when comparing it to a reference (i.e., native) protein structure [60]. The quality of a protein structure is reported as a single scalar value representing a method’s predicted global distance test (GDT_TS) score [82] between the provided decoy structure and the native structure. Such information is crucial in drug discovery efforts when one is tasked with designing a drug (e.g., ligand) that should bind to a particular protein target, notably when such targets have not yet had their 3D structures experimentally determined and have rather had them predicted computationally using methods such as AlphaFold 2 [42]. The respective dataset for this SE(3)-invariant

task is also derived from the ATOM3D dataset [60] and is comprised of 40,950 decoy structures corresponding to 649 total targets, where cross-validation splits are created according to a target’s release year in the Critical Assessment of Techniques for Protein Structure Prediction (CASP) competition [83]. Results are reported in terms of the Pearson’s correlation (p), Spearman’s correlation (Sp), and Kendall’s tau correlation (K) between a method’s predictions on the test dataset and the corresponding ground-truth GDT_TS values, where local results are averaged across predictions for individual targets and global results are averaged directly across all targets. Baseline comparison methods for this task include a composition of state-of-the-art CNNs, GNNs, and ENNs, as well as previous statistics-based methods.

Conveying a similar message to that in Table 2, the results in Table 3 demonstrate that, in operating on atom-level protein graphs, GCPNET performs best against all other state-of-the-art models for the task of estimating a 3D protein structure’s quality (i.e., PSR). In this setting, GCPNET outperforms all other methods across all local and global metrics by 2.5% on average. Once again, GCPNET’s predictions are highly statistically significant, this time with Pearson, Spearman, and Kendall tau p-values all below $1e - 50$, respectively.

Identifying components for effective protein structure ranking. Our ablation studies with GCPNET, in the context of PSR, once more reveal that the design of our local frames, RESGCP module, and scalar and vector feature channels are all beneficial for enhancing GCPNet’s ability to analyze a given 3D graph input. Here, in sensitizing the model to chemical chirality, our local frame embeddings improve GCPNET’s performance for PSR by 4% on average. Similarly, our RESGCP module improves the model’s performance by 5%. Interestingly, without access to scalar-valued node and edge features, GCPNET is unable to produce valid predictions for the PSR test dataset due to what appears to be a phenomenon of vector-wise latent variable collapse [84]. This finding suggests that, for the PSR task, the baseline GCPNET model relies strongly on the scalar-valued representations it produces. Lastly, including vector-valued features within GCPNET improves the model’s performance for the PSR task by 9%.

Evaluating trajectory predictions for Newtonian many-body systems. Newtonian many-body systems modeling (NMS) asks methods to forecast the future positions of particles in many-body systems of various sizes [53], bridging the gap between the domains of machine learning and physics. In our experimental results for the NMS task, the four systems (i.e., datasets) on which we evaluate each method are comprised of increasingly more nodes and are influenced by force fields of increasingly complex directional origins for which to model, namely electrostatic force fields for 5-body (ES(5)) and 20-body (ES(20)) systems as well as for 20-body systems under the influence of an additional gravity field (G+ES(20)) and Lorentz-like force field (L+ES(20)), respectively. The four datasets for this SE(3)-equivariant task were generated using the descriptions and source code of [53], where each dataset is comprised of 7,000 total trajectories. Results are reported in terms of the mean squared error (MSE) between a method’s node position predictions on the test dataset and the corresponding ground-truth node positions after 1,000 timesteps. Baseline comparison methods for this task include a collection of state-of-the-art GNNs, ENNs, and Transformers.

Table 4: Comparison of GCPNET with baseline methods for the NMS task. Results are reported in terms of the MSE for future position prediction over four test datasets of increasing modeling difficulty, graph sizes, and composed force field complexities. The final column reports each method’s MSE averaged across all four test datasets. The best results for this task are in **bold**, and the second-best results are underlined. N/A denotes an experiment that could not be performed due to a method’s numerical instability.

Method	ES(5)	ES(20)	G+ES(20)	L+ES(20)	Average
GNN [2022]	0.0131	0.0720	0.0721	0.0908	0.0620
TFN [2022]	0.0236	0.0794	0.0845	0.1243	0.0780
SE(3)-Transformer [2022]	0.0329	0.1349	0.1000	0.1438	0.1029
Radial Field [2022]	0.0207	0.0377	0.0399	0.0779	0.0441
PaiNN [2021]	0.0158	N/A	N/A	N/A	N/A
ET [2022]	0.1653	0.1788	0.2122	0.2989	0.2138
EGNN [2022]	0.0079	0.0128	0.0118	0.0368	0.0173
ClofNet [2022]	0.0065	<u>0.0073</u>	0.0072	0.0251	0.0115
GCPNET w/o Frames	<u>0.0067</u>	0.0074	0.0074	<u>0.0200</u>	<u>0.0103</u>
GCPNET w/o ResGCP	0.0090	0.0135	0.0099	0.0278	0.0150
GCPNET w/o Scalars	0.0119	0.0173	0.0170	0.0437	0.0225
GCPNET	0.0070	0.0071	<u>0.0073</u>	0.0173	0.0097

The results in Table 4 show that GCPNET achieves the lowest MSE averaged across all four NMS datasets, improving upon the state-of-the-art MSE for trajectory predictions in this task by 19% on average. In particular, GCPNET achieves the best results for two of the four NMS datasets considered in this work, where these two datasets are respectively the first and third most difficult NMS datasets for methods to model. On the two remaining datasets, GCPNET matches the performance of prior state-of-the-art methods. Moreover, across all four datasets, GCPNET’s trajectory predictions yield an RMSE of 0.0963 and achieve Pearson, Spearman, and Kendall’s tau correlations of 0.999, 0.999, and 0.981, respectively, where all such correlation values are highly statistically significant (i.e., p-values $< 1e - 50$). Note that, to calculate these correlation values, we score GCPNET’s vector-valued predictions independently for each coordinate axis and then average the resulting metrics.

Analyzing components for successful trajectory forecasting. Once again, our ablation studies with GCPNET demonstrate the importance of GCPNET’s local frame embeddings, scalar information, and ResGCP module. Here, we note that we were not able to include an ablation study on GCPNET’s vector-valued features since they are directly used to predict node position displacements for trajectory forecasting. Table 4 shows that each model component synergistically enables GCPNET to achieve new state-of-the-art results for the NMS task. In enabling the model to detect global forces, our proposed local frame embeddings improve GCPNET’s ability to learn many-body system dynamics by 6% on average across all dataset contexts. Specifically interesting to note is that these local frame embeddings improve the model’s trajectory predictions within the most complex dataset context (i.e., L+ES(20)) by

14%, suggesting that such frame embeddings improve GCPNET’s ability to learn many-body system dynamics even in the presence of complex global force fields. Furthermore, GCPNET’s RESGCP module and scalar-valued features improve the model’s performance for modeling many-body systems by 35% and 57%, respectively.

Across all tasks studied in this work, GCPNET improves upon the overall performance of all previous methods. Our experiments demonstrate this for both node-level (e.g., NMS) and graph-level (e.g., LBA) prediction tasks, verifying GCPNET’s ability to encode useful information for both scales of granularity. Furthermore, we have demonstrated the importance of each model component within GCPNET, showing how these components are complementary to each other in the context of representation learning over 3D molecular data. We will now proceed to describe the design and operations of our proposed GCPNET model architecture.

3 Methods

3.1 Preliminaries

3.1.1 Overview of the Problem Setting

We represent a 3D molecular structure as a 3D k -nearest neighbors (k -NN) graph $\mathcal{G} = (\mathcal{V}, \mathcal{E})$ with \mathcal{V} and \mathcal{E} representing the graph’s set of nodes and set of edges, respectively, and $N = |\mathcal{V}|$ and $E = |\mathcal{E}|$ representing the number of nodes and the number of edges in the graph, respectively. In addition, $\mathbf{X} \in \mathbb{R}^{N \times 3}$ represents the respective Cartesian coordinates for each node. We then design E(3)-invariant (i.e., 3D rotation, reflection, and translation-invariant) node features $\mathbf{H} \in \mathbb{R}^{N \times h}$ and edge features $\mathbf{E} \in \mathbb{R}^{E \times e}$ as well as O(3)-equivariant (3D rotation and reflection-equivariant) node features $\boldsymbol{\chi} \in \mathbb{R}^{N \times (m \times 3)}$ and edge features $\boldsymbol{\xi} \in \mathbb{R}^{E \times (x \times 3)}$, respectively.

Upon constructing such features, we apply several layers of graph message-passing using a neural network Φ (which later on we refer to as GCPNET) that updates node and edge features using invariant and equivariant representations for the corresponding feature types. Importantly, Φ guarantees, by design, $SE(3)$ *equivariance* with respect to its vector-valued input coordinates and features (i.e., $x_i \in \mathbf{X}$, $\chi_i \in \boldsymbol{\chi}$, and $\xi_{ij} \in \boldsymbol{\xi}$) and $SE(3)$ -*invariance* regarding its scalar features (i.e., $h_i \in \mathbf{H}$ and $e_{ij} \in \mathbf{E}$). In addition, Φ ’s scalar graph representations achieve *geometric self-consistency* for the 3D structure of the input molecular graph \mathcal{G} , sensitizing them to the effects of molecular chirality while making them uniquely identifiable under 3D rotations. Lastly, geometric completeness requires methods that accept 3D molecular graph inputs to be able to discern the local geometric environment of a given atom with no directional ambiguities. This enables geometry-complete methods such as Φ to detect the presence and influence of global force fields acting on the graph inputs. We formalize these equivariance, geometric self-consistency, and geometric completeness constraints using the three following definitions, where \square' represents a feature that has been updated by our neural network.

Definition 1. (*SE(3) Equivariance*).

Given $(\mathbf{H}', \mathbf{E}', \mathbf{X}', \boldsymbol{\chi}', \boldsymbol{\xi}') = \Phi(\mathbf{H}, \mathbf{E}, \mathbf{X}, \boldsymbol{\chi}, \boldsymbol{\xi})$, we have
 $(\mathbf{H}', \mathbf{E}', \mathbf{Q}\mathbf{X}'^T + \mathbf{g}, \mathbf{Q}\boldsymbol{\chi}'^T, \mathbf{Q}\boldsymbol{\xi}'^T) = \Phi(\mathbf{H}, \mathbf{E}, \mathbf{Q}\mathbf{X}^T + \mathbf{g}, \mathbf{Q}\boldsymbol{\chi}^T, \mathbf{Q}\boldsymbol{\xi}^T)$,
 $\forall \mathbf{Q} \in SO(3), \forall \mathbf{g} \in \mathbb{R}^{3 \times 1}$.

Definition 2. (*Geometric Self-Consistency*).

Given a pair of molecular graphs \mathcal{G}_1 and \mathcal{G}_2 ,
with $\mathbf{X}^1 = \{\mathbf{x}_i^1\}_{i=1, \dots, N}$ and $\mathbf{X}^2 = \{\mathbf{x}_i^2\}_{i=1, \dots, N}$, respectively,
a geometric representation $\Phi(\mathbf{H}, \mathbf{E}) = \Phi(\mathcal{G})$ is considered
geometrically self-consistent if $\Phi(\mathcal{G}^1) = \Phi(\mathcal{G}^2) \iff \exists \mathbf{Q} \in SO(3), \exists \mathbf{g} \in \mathbb{R}^{3 \times 1}$,
for $i = 1, \dots, n, \mathbf{X}_i^{1T} = \mathbf{Q}\mathbf{X}_i^{2T} + \mathbf{g}$ [85].

Definition 3. (*Geometric Completeness*).

Given a positional pair of nodes (x_i^t, x_j^t) in a 3D graph \mathcal{G} ,
with vectors $a_{ij}^t \in \mathbb{R}^{1 \times 3}$, $b_{ij}^t \in \mathbb{R}^{1 \times 3}$, and $c_{ij}^t \in \mathbb{R}^{1 \times 3}$ derived from (x_i^t, x_j^t) ,
a local geometric representation $\mathcal{F}_{ij}^t = (a_{ij}^t, b_{ij}^t, c_{ij}^t) \in \mathbb{R}^{3 \times 3}$ is considered
geometrically complete if \mathcal{F}_{ij}^t is non-degenerate, thereby forming a
local orthonormal basis located at the tangent space of x_i^t [53].

3.1.2 SE(3)-equivariant complete representations

Representation learning on 3D molecular structures is a challenging task for a variety of reasons: (1) an expressive representation learning model should be able to predict arbitrary vector-valued quantities for each atom and atom pair in the molecular structure (e.g., using $\boldsymbol{\chi}'$ and $\boldsymbol{\xi}'$ to predict side-chain atom positions and atom-atom displacements for each residue in a 3D protein graph); (2) arbitrary rotations or translations to a 3D molecular structure should affect only the vector-valued representations a model assigns to a molecular graph’s nodes or edges, whereas such 3D transformations of the molecular structure should not affect the model’s scalar representations for nodes and edges [53]; (3) the geometrically invariant properties of a molecule’s 3D structure should be uniquely identifiable by a model; and (4) in a geometry-complete manner, scalar and vector-valued representations should mutually exchange information between nodes and edges during a model’s forward pass for a 3D input graph, as these information types can be correlatively related (e.g., a scalar feature such as the L_2 norm of a vector v can be associated with the vector of origin v) [41, 54].

In line with this reasoning, we need to ensure that the coordinates our model predicts for the node positions in a molecular graph \mathcal{G} transform according to SE(3) transformations of the input positions. This runs in contrast to previous methods that remain strictly E(3)-equivariant or E(3)-invariant to 3D transformations of the input \mathcal{G} and consequently ignore the important effects of molecular chirality. At the same time, the model should jointly update the scalar and vector-valued features of \mathcal{G} according to their respective molecular symmetry groups to increase the model’s expressiveness in approximating geometric and physical quantities [86]. To increase its generalization capabilities, the model should also disambiguate any *geometric directions* within its

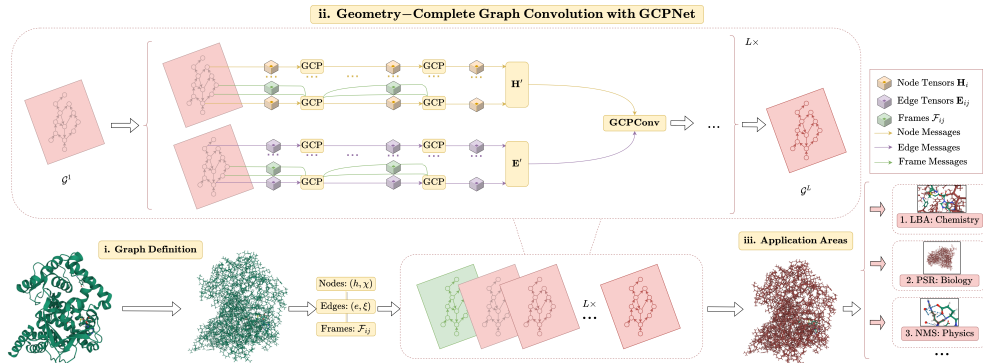


Fig. 2: A framework overview for our proposed *Geometry-Complete Perceptron Network* (GCPNET). Our framework consists of (i.) a graph (topology) definition process, (ii.) a GCPNET-based graph neural network for 3D molecular representation learning, and (iii.) demonstrated application areas for GCPNET. Zoom in for the best viewing experience.

local node environments and should maintain $SE(3)$ -invariance of its scalar representations when the input graph is transformed in 3D space. Following [70], this helps prevent the model from losing important geometric or chiral information (i.e., becoming geometrically self-inconsistent) during graph message-passing. One way to do this is to introduce a new type of message-passing neural network.

3.2 GCPNet Model Architecture

Towards this end, we introduce our architecture for Φ satisfying Defs. (1), (2), and (3) which we refer to as the Geometry-Complete $SE(3)$ -Equivariant Perceptron Network (GCPNET). We illustrate the GCPNET algorithm in Figure 2 and outline it in Algorithm 1. Subsequently, we expand on our definition for **GCP** and **GCPConv** in Sections 3.2.1 and 3.3.1, respectively, while further illustrating **GCP** in Figure 3.

We can then prove the following three propositions (see Appendices A.1 through A.3 for a more detailed description of the GCPNET algorithm and its equivariant properties).

- **Proposition 1.** GCPNETS are $SE(3)$ -equivariant
 \rightarrow Def. (1).
- **Proposition 2.** GCPNETS are geometry self-consistent
 \rightarrow Def. (2).
- **Proposition 3.** GCPNETS are geometry-complete
 \rightarrow Def. (3).

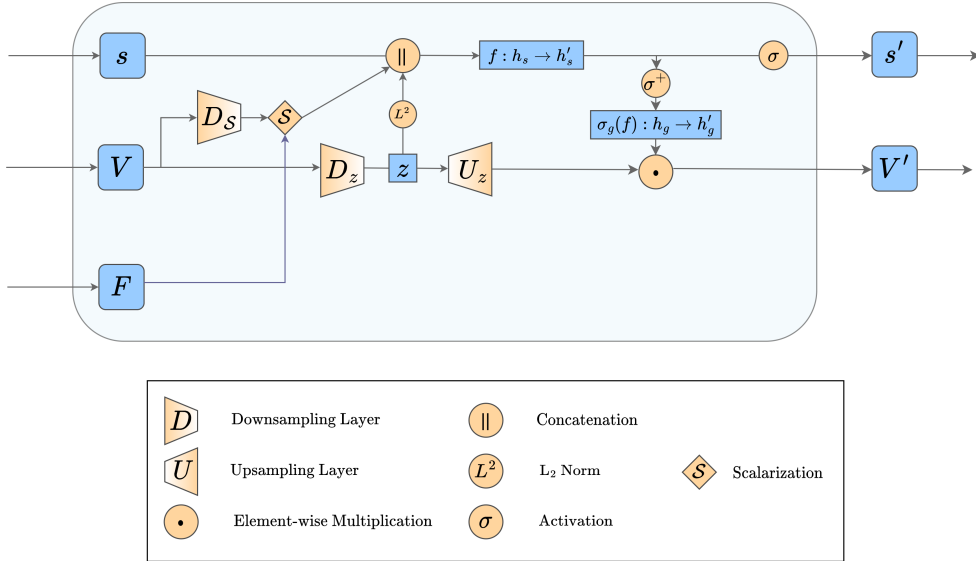


Fig. 3: An overview of our proposed Geometry-Complete Perceptron (**GCP**) module. The **GCP** module introduces node and edge-centric encodings of 3D frames as input features that are used to directly update both scalar and vector-valued features with geometric information-completeness guarantees as well as chirality sensitivity.

3.2.1 Geometry-Complete Perceptron Module

As illustrated in Figure 3, GCPNET represents the features for nodes within an input graph as a tuple (h, χ) to distinguish scalar features ($h \in \mathbb{R}^h$) from vector-valued features ($\chi \in \mathbb{R}^{m \times 3}$). Similarly, GCPNET represents an input graph’s edge features as a tuple (e, ξ) to differentiate scalar features ($e \in \mathbb{R}^e$) from vector-valued features ($\xi \in \mathbb{R}^{x \times 3}$). For conciseness, we will subsequently refer to both node and edge feature tuples as (s, V) . We then define $\mathbf{GCP}_{\mathcal{F}_{ij}, \lambda}(\cdot)$ to represent the **GCP** encoding process, where λ represents a downscaling hyperparameter (e.g., 3) and $\mathcal{F}_{ij} \in \mathbb{R}^{3 \times 3}$ denotes the SO(3)-equivariant (i.e., 3D rotation-equivariant) frames constructed using the **Localize** operation (i.e., the **EquiFrame** operation of [53]) in Algorithm 1. Specifically, the frame encodings are defined as $\mathcal{F}_{ij}^t = (a_{ij}^t, b_{ij}^t, c_{ij}^t)$, with $a_{ij}^t = \frac{x_i^t - x_j^t}{\|x_i^t - x_j^t\|}$, $b_{ij}^t = \frac{x_i^t \times x_j^t}{\|x_i^t \times x_j^t\|}$, and $c_{ij}^t = a_{ij}^t \times b_{ij}^t$, respectively. In Appendix A.3, we discuss how these frame encodings are direction information-complete for edges, allowing networks incorporating them to effectively detect and leverage for downstream tasks the force fields present within real-world many-body systems such as small molecules and proteins.

Expressing Vector Representations with V . The **GCP** module then expresses vector representations V as follows. The features V with representation depth r are downscaled by λ .

$$z = \{v \mathbf{w}_{d_z} | \mathbf{w}_{d_z} \in \mathbb{R}^{r \times (r/\lambda)}\} \quad (1)$$

Additionally, V is separately downscaled in preparation to be subsequently embedded as direction-sensitive edge scalar features.

$$V_s = \{v\mathbf{w}_{d_s} | \mathbf{w}_{d_s} \in \mathbb{R}^{r \times (3 \times 3)}\} \quad (2)$$

Deriving Scalar Representations s' . To update scalar representations, the **GCP** module, in the following manner, derives two invariant sources of information from V and combines them with s :

$$q_{ij} = (V_s \cdot \mathcal{F}_{ij}) \in \mathbb{R}^9 \quad (3)$$

$$q = \begin{cases} \frac{1}{|\mathcal{N}(i)|} \sum_{j \in \mathcal{N}(i)} q_{ij} & \text{if } V_s \text{ represents nodes} \\ q_{ij} & \text{if } V_s \text{ represents edges} \end{cases} \quad (4)$$

$$s_{(s,q,z)} = s \cup q \cup \|z\|_2 \quad (5)$$

where \cdot denotes the inner product, $\mathcal{N}(\cdot)$ represents the neighbors of a node, and $\|\cdot\|_2$ denotes the L_2 norm. Then, denote t as the representation depth of s , and let $s_{(s,q,z)} \in \mathbb{R}^{t+9+(r/\lambda)}$ with representation depth $(t+9+(r/\lambda))$ be projected to s' with representation depth t' :

$$s_v = \{s_{(s,q,z)}\mathbf{w}_s + \mathbf{b}_s | \mathbf{w}_s \in \mathbb{R}^{(t+9+(r/\lambda)) \times t'}\} \quad (6)$$

$$s' = \sigma_s(s_v) \quad (7)$$

Note that embedding geometric frames \mathcal{F}_{ij} as q_{ij} in Equation 3 ultimately enables GCPNET to iteratively learn chirality-sensitive and global force-aware representations of each 3D network input. Moreover, Equation 4 allows GCPNET to encode local geometric substructures for each node, where the theoretical importance of such network behavior is discussed in detail by [87].

Deriving Vector Representations V' . The **GCP** module then concludes by updating vector representations as follows:

$$V_u = \{z\mathbf{w}_{u_z} | \mathbf{w}_{u_z} \in \mathbb{R}^{(r/\lambda) \times r'}\} \quad (8)$$

$$V' = \{V_u \odot \sigma_g(\sigma^+(s_v)\mathbf{w}_g + \mathbf{b}_g) | \mathbf{w}_g \in \mathbb{R}^{t' \times r'}\} \quad (9)$$

where \odot represents element-wise multiplication and the gating function σ_g is applied row-wise to preserve $\text{SO}(3)$ equivariance within V' .

Conceptually, the **GCP** module is autoregressively applied to tuples (s, V) a total of ω times to derive rich scalar and vector-valued features. The module does so by blending both feature types iteratively with the 3D direction and information completeness guarantees provided by geometric frame encodings \mathcal{F}_{ij} . We note that this model design runs in contrast with prior graph neural networks for physical systems such as GVP-GNNs [53] and ClofNet [46], which are either insensitive to chemical

chirality and global atomic forces or do not directly learn geometric features for downstream prediction tasks, making the proposed **GCP** module well suited for learning directly from 3D molecular graphs.

3.3 Learning from 3D Graphs with GCPNet

In this section, we propose a flexible manner in which to perform 3D graph convolution with our proposed **GCP** module, as illustrated in Figure 2 and employed in Algorithm 1.

3.3.1 Geometry-Complete Graph Convolution.

Let $\mathcal{N}(i)$ denote the neighbors of node n_i , selected using a distance-based metric such as k-nearest neighbors or a radial distance cutoff. Subsequently, we define a single layer l of geometry-complete graph convolution as

$$n_i^l = \phi^l(n_i^{l-1}, \mathcal{A}_{\forall j \in \mathcal{N}(i)} \Omega_\omega^l(n_i^{l-1}, n_j^{l-1}, e_{ij}, \mathcal{F}_{ij})), \quad (10)$$

where $n_i^l = (h_i^l, \chi_i^l)$; $e_{ij} = (e_{ij}^0, \xi_{ij}^0)$; Φ is a trainable function denoted as **GCPConv**; l signifies the representation depth of the network; \mathcal{A} is a permutation-invariant aggregation function; and Ω_ω represents a message-passing function corresponding to the ω -th **GCP** message-passing layer. We proceed to expand on the operations of each graph convolution layer as follows.

To start, messages between source nodes i and neighboring nodes j are first constructed as

$$m_{ij}^0 = \mathbf{GCP}(n_i^0 \cup n_j^0 \cup e_{ij}, \mathcal{F}_{ij}) \quad (11)$$

where \cup denotes a concatenation operation. Then, up to the ω -th iteration, each message is updated by the m -th message update layer using residual connections as

$$\Omega_\omega^l = \mathbf{ResGCP}_\omega^l(m_{ij}^{l-1}, \mathcal{F}_{ij}), \quad (12)$$

$$\mathbf{ResGCP}_\eta^l(z_i^{l-1}, \mathcal{F}_{ij}) = z_i^{l-1} + \mathbf{GCP}_\eta^l(z_i^{l-1}, \mathcal{F}_{ij}), \quad (13)$$

where we empirically find such residual connections between message representations to reduce oversmoothing within GCPNET by mitigating the problem of vanishing gradients.

Updated node features \hat{n}^l are then derived residually using an aggregation of generated messages as

$$\hat{n}^l = n^{l-1} + f(\{\Omega_{\omega, v_i}^l | v_i \in \mathcal{V}\}), \quad (14)$$

where f represents an aggregation function such as a summation or mean that is invariant to permutations of node ordering. The residual connection between \hat{n}^l and n^l is established here to encourage the network to update the representation space of node features in a layer-asynchronous manner.

To encourage GCPNET to make its node feature representations independent of the size of each input graph, we then employ a node-centric feed-forward network to

Algorithm 1 GCPNET

```
1: Input:  $(h_i \in \mathbf{H}, \chi_i \in \mathbf{X}), (e_{ij} \in \mathbf{E}, \xi_{ij} \in \mathbf{\xi}),$   
    $x_i \in \mathbf{X},$  graph  $\mathcal{G}$   
2: Initialize  $\mathbf{X}^0 = \mathbf{X}^C \leftarrow \mathbf{Centralize}(\mathbf{X})$   
3:  $\mathcal{F}_{ij} = \mathbf{Localize}(x_i \in \mathbf{X}^0, x_j \in \mathbf{X}^0)$   
4: Project  $(h_i^0, \chi_i^0), (e_{ij}^0, \xi_{ij}^0) \leftarrow \mathbf{GCP}_e((h_i, \chi_i), (e_{ij}, \xi_{ij}), \mathcal{F}_{ij})$   
5: for  $l = 1$  to  $L$  do  
6:    $(h_i^l, \chi_i^l), x_i^l = \mathbf{GCPConv}^l((h_i^{l-1}, \chi_i^{l-1}), (e_{ij}^0, \xi_{ij}^0), x_i^{l-1}, \mathcal{F}_{ij})$   
7: end for  
8: if Updating Node Positions then  
9:    $\mathcal{F}_{ij}^L = \mathbf{Localize}(x_i \in \mathbf{X}^L, x_j \in \mathbf{X}^L)$   
10:  Finalize  $(\mathbf{X}^L) \leftarrow \mathbf{Decentralize}(\mathbf{X}^L)$   
11: else  
12:   $x_i^L = x_i^0$   
13: end if  
14: Project  $(h_i^L, \chi_i^L), (e_{ij}^L, \xi_{ij}^L) \leftarrow \mathbf{GCP}_p((h_i^l, \chi_i^l), (e_{ij}^0, \xi_{ij}^0), \mathcal{F}_{ij}^L)$   
15: Output:  $(h_i^L, \chi_i^L), (e_{ij}^L, \xi_{ij}^L), x_i^L$ 
```

update node representations. Specifically, we apply to \hat{n}^l a linear **GCP** function with shared weights ϕ_f followed by r **ResGCP** modules, operations concisely portrayed as

$$\tilde{n}_{r-1}^l = \phi_f^l(\hat{n}^l) \quad (15)$$

$$n^l = \mathbf{ResGCP}_r^l(\tilde{n}_{r-1}^l). \quad (16)$$

Lastly, if one desires to update the positions of each node in \mathcal{G} (e.g., as we do for tasks involving position-related predictions such as NMS), we propose a flexible, SE(3)-equivariant method to do so using a dedicated **GCP** module as follows:

$$(h_{p_i}^l, \chi_{p_i}^l) = \mathbf{GCP}_p^l(n_i^l, \mathcal{F}_{ij}) \quad (17)$$

$$x_i^l = x_i^{l-1} + \chi_{p_i}^l, \text{ where } \chi_{p_i}^l \in \mathbb{R}^{1 \times 3}. \quad (18)$$

3.3.2 The GCPNet Algorithm

In this section, we describe our overall learning algorithm driven by GCPNET (Algorithm 1). We also discuss the rationale behind our design decisions for GCPNET and provide examples of use cases in which one might apply GCPNET for specific learning tasks.

On Line 2 of Algorithm 1, the **Centralize** operation removes the center of mass from each node position in the input graph to ensure that such positions are subsequently 3D translation-invariant.

Thereafter, following [53], the **Localize** operation on Line 3 crafts translation-invariant and SO(3)-equivariant frame encodings $\mathcal{F}_{ij}^t = (a_{ij}^t, b_{ij}^t, c_{ij}^t)$. As described in more detail in Appendix A.3, these frame encodings are chirality-sensitive and direction information-complete for edges, imbuing networks that incorporate them

with the ability to more easily detect force field interactions present in many real-world atomic systems, as we demonstrate through corresponding experiments in Section 2.

Before applying any geometry-complete graph convolution layers, on Line 4 we use \mathbf{GCP}_e to embed our input node and edge features into scalar and vector-valued values, respectively, while incorporating geometric frame information. Subsequently, in Lines 5-6, each layer of geometry-complete graph convolution is performed autoregressively via $\mathbf{GCPConv}^l$ starting from these initial node and edge feature embeddings, all while maintaining information flow originating from the geometric frames \mathcal{F}_{ij} .

On Lines 8 through 12, we finalize our procedure with which to update in an SE(3)-equivariant manner the position of each node in an input 3D graph. In particular, we update node positions by residually adding learned vector-valued node features ($\chi_{v_i}^l$) to the node positions produced by the previous $\mathbf{GCPConv}$ layer ($l-1$). As shown in Appendix A.1, such updates are initially SO(3)-equivariant, and on Line 10 we ensure these updates also become 3D translation-equivariant by adding back to each node position the input graph’s original center of mass via the **Decentralize** operation. In total, this procedure produces SE(3)-equivariant updates to node positions. Additionally, for models that update node positions, we note that Line 9 updates frame encodings \mathcal{F}_{ij} using the model’s final predictions for node positions to provide more information-rich feature projections on Line 14 via \mathbf{GCP}_p to conclude the forward pass of GCPNET.

3.3.3 Network Utilities.

In summary, GCPNET receives an input 3D graph \mathcal{G} with node positions \mathbf{x} , scalar node and edge features, h and e , as well as vector-valued node and edge features, χ and ξ . The model is then capable of e.g., (1) predicting scalar node, edge, or graph-level properties while maintaining SE(3) invariance; (2) estimating vector-valued node, edge, or graph-level properties while ensuring SE(3) equivariance; or (3) updating node positions in an SE(3)-equivariant manner.

4 Discussion

In light of our impressive results with GCPNET, future work on the model could involve researching more computationally-efficient variations of GCPNET that require fewer GCP message-passing layers within each GCP convolution layer or that embed geometric frames sparsely rather than in each GCP layer. Interestingly, [87] recently showed that GCPNET, in particular, is theoretically robust in terms of its geometric expressiveness of local geometric substructures and global geometric interaction terms. Nonetheless, [87] also highlight future directions for improving such methods’ expressiveness for learning equivariant-valued features including incorporating higher-order equivariant tensors into one’s message-passing procedure. Enhancing its geometric expressiveness to thereby increase its runtime efficiency would allow GCPNET to be used increasingly in new scientific and deep learning applications requiring high computational throughput (e.g., virtual screening of new drugs).

5 Conclusion

In this work, we introduced GCPNET, a state-of-the-art GNN for 3D molecular graph representation learning. We have demonstrated its utility through several benchmark studies. In future work, we aim to develop extensions of GCPNET that increase its geometric expressiveness as well as explore applications of GCPNET for generative modeling of molecular structures.

Code Availability. The source code for GCPNET is available at <https://github.com/BioinfoMachineLearning/GCPNet>.

Data Availability. The data required to train new GCPNET models or reproduce our results for the NMS task are available under a Creative Commons Attribution 4.0 International Public License at <https://zenodo.org/record/7293186>. The data required to train new GCPNET models or reproduce our results for the RS task are available under an MIT License at <https://figshare.com/s/e23be65a884ce7fc8543>. All other data required to train new GCPNET models or reproduce our results for the remaining tasks are available to download using our model training scripts available at <https://github.com/BioinfoMachineLearning/GCPNet>.

Acknowledgments. This work is partially supported by two NSF grants (DBI1759934 and IIS1763246), two NIH grants (R01GM093123 and R01GM146340), three DOE grants (DE-AR0001213, DE-SC0020400, and DE-SC0021303), and the computing allocation on the Summit compute cluster provided by the Oak Ridge Leadership Computing Facility.

Author Contributions Statement. AM and JC conceived the project. AM designed the experiments. AM performed the experiments and collected the data. AM analyzed the data. AM and JC wrote the manuscript. AM and JC edited the manuscript.

Competing Interests Statement. The authors declare no competing interests.

References

- [1] Sehnal, D., Bittrich, S., Deshpande, M., Svobodová, R., Berka, K., Bazgier, V., Velankar, S., Burley, S.K., Koča, J., Rose, A.S.: Mol* viewer: modern web app for 3d visualization and analysis of large biomolecular structures. *Nucleic Acids Research* **49**(W1), 431–437 (2021)
- [2] Valsesia, D., Fracastoro, G., Magli, E.: Learning localized generative models for 3d point clouds via graph convolution. In: *International Conference on Learning Representations* (2018)
- [3] Qi, X., Liao, R., Jia, J., Fidler, S., Urtasun, R.: 3d graph neural networks for rgb-d semantic segmentation. In: *Proceedings of the IEEE International Conference on Computer Vision*, pp. 5199–5208 (2017)

- [4] Zhang, Y., Rabbat, M.: A graph-cnn for 3d point cloud classification. In: 2018 IEEE International Conference on Acoustics, Speech and Signal Processing (ICASSP), pp. 6279–6283 (2018). IEEE
- [5] Zhou, H., Feng, Y., Fang, M., Wei, M., Qin, J., Lu, T.: Adaptive graph convolution for point cloud analysis. In: Proceedings of the IEEE/CVF International Conference on Computer Vision, pp. 4965–4974 (2021)
- [6] Esteves, C.: Theoretical aspects of group equivariant neural networks. arXiv preprint arXiv:2004.05154 (2020)
- [7] Hegyi, H., Gerstein, M.: The relationship between protein structure and function: a comprehensive survey with application to the yeast genome. *Journal of molecular biology* **288**(1), 147–164 (1999)
- [8] Umulis, D.M., Othmer, H.G.: The importance of geometry in mathematical models of developing systems. *Current opinion in genetics & development* **22**(6), 547–552 (2012)
- [9] Matter, F., Niederberger, M.: The importance of the macroscopic geometry in gas-phase photocatalysis. *Advanced Science* **9**(13), 2105363 (2022)
- [10] Hamilton, W.L.: Graph representation learning. *Synthesis Lectures on Artificial Intelligence and Machine Learning* **14**(3), 1–159 (2020)
- [11] Cao, W., Zheng, C., Yan, Z., He, Z., Xie, W.: Geometric machine learning: research and applications. *Multimedia Tools and Applications*, 1–53 (2022)
- [12] Masci, J., Rodolà, E., Boscaini, D., Bronstein, M.M., Li, H.: Geometric deep learning. In: SIGGRAPH ASIA 2016 Courses. SA '16. Association for Computing Machinery, New York, NY, USA (2016). <https://doi.org/10.1145/2988458.2988485> . <https://doi.org/10.1145/2988458.2988485>
- [13] Bronstein, M.M., Bruna, J., LeCun, Y., Szlam, A., Vandergheynst, P.: Geometric deep learning: going beyond euclidean data. *IEEE Signal Processing Magazine* **34**(4), 18–42 (2017)
- [14] Bronstein, M.M., Bruna, J., Cohen, T., Velicković, P.: Geometric deep learning: Grids, groups, graphs, geodesics, and gauges. arXiv preprint arXiv:2104.13478 (2021)
- [15] Cao, W., Yan, Z., He, Z., He, Z.: A comprehensive survey on geometric deep learning. *IEEE Access* **8**, 35929–35949 (2020)
- [16] Kiarashinejad, Y., Zandehshahvar, M., Abdollahramezani, S., Hemmatyar, O., Pourabolghasem, R., Adibi, A.: Knowledge discovery in nanophotonics using geometric deep learning. *Advanced Intelligent Systems* **2**(2), 1900132 (2020)

- [17] James, J.: Citywide traffic speed prediction: A geometric deep learning approach. *Knowledge-Based Systems* **212**, 106592 (2021)
- [18] LeCun, Y., Bengio, Y., *et al.*: Convolutional networks for images, speech, and time series. *The handbook of brain theory and neural networks* **3361**(10), 1995 (1995)
- [19] He, K., Zhang, X., Ren, S., Sun, J.: Deep residual learning for image recognition. In: *Proceedings of the IEEE Conference on Computer Vision and Pattern Recognition*, pp. 770–778 (2016)
- [20] He, K., Gkioxari, G., Dollár, P., Girshick, R.: Mask r-cnn. In: *Proceedings of the IEEE International Conference on Computer Vision*, pp. 2961–2969 (2017)
- [21] Krizhevsky, A., Sutskever, I., Hinton, G.E.: Imagenet classification with deep convolutional neural networks. *Communications of the ACM* **60**(6), 84–90 (2017)
- [22] Kipf, T.N., Welling, M.: Semi-supervised classification with graph convolutional networks. *arXiv preprint arXiv:1609.02907* (2016)
- [23] Gilmer, J., Schoenholz, S.S., Riley, P.F., Vinyals, O., Dahl, G.E.: Neural message passing for quantum chemistry. In: *International Conference on Machine Learning*, pp. 1263–1272 (2017). PMLR
- [24] Veličković, P., Cucurull, G., Casanova, A., Romero, A., Lio, P., Bengio, Y.: Graph attention networks. *arXiv preprint arXiv:1710.10903* (2017)
- [25] Dwivedi, V.P., Bresson, X.: A generalization of transformer networks to graphs. *arXiv preprint arXiv:2012.09699* (2020)
- [26] Qi, C.R., Su, H., Mo, K., Guibas, L.J.: Pointnet: Deep learning on point sets for 3d classification and segmentation. In: *Proceedings of the IEEE Conference on Computer Vision and Pattern Recognition*, pp. 652–660 (2017)
- [27] Liu, Y., Fan, B., Xiang, S., Pan, C.: Relation-shape convolutional neural network for point cloud analysis. In: *Proceedings of the IEEE/CVF Conference on Computer Vision and Pattern Recognition*, pp. 8895–8904 (2019)
- [28] Zhang, Z., Hua, B.-S., Yeung, S.-K.: Shellnet: Efficient point cloud convolutional neural networks using concentric shells statistics. In: *Proceedings of the IEEE/CVF International Conference on Computer Vision*, pp. 1607–1616 (2019)
- [29] Graves, A., Mohamed, A.-r., Hinton, G.: Speech recognition with deep recurrent neural networks. In: *2013 IEEE International Conference on Acoustics, Speech and Signal Processing*, pp. 6645–6649 (2013). Ieee
- [30] Graves, A., Jaitly, N.: Towards end-to-end speech recognition with recurrent neural networks. In: *International Conference on Machine Learning*, pp. 1764–1772

- (2014). PMLR
- [31] Hughes, T.W., Williamson, I.A., Minkov, M., Fan, S.: Wave physics as an analog recurrent neural network. *Science advances* **5**(12), 6946 (2019)
 - [32] Duvenaud, D.K., Maclaurin, D., Iparraguirre, J., Bombarell, R., Hirzel, T., Aspuru-Guzik, A., Adams, R.P.: Convolutional networks on graphs for learning molecular fingerprints. In: Cortes, C., Lawrence, N., Lee, D., Sugiyama, M., Garnett, R. (eds.) *Advances in Neural Information Processing Systems*, vol. 28. Curran Associates, Inc., ??? (2015). <https://proceedings.neurips.cc/paper/2015/file/f9be311e65d81a9ad8150a60844bb94c-Paper.pdf>
 - [33] Liu, Y., Wang, L., Liu, M., Zhang, X., Oztekin, B., Ji, S.: Spherical message passing for 3d graph networks. *arXiv preprint arXiv:2102.05013* (2021)
 - [34] Akutsu, T., Nagamochi, H.: Comparison and enumeration of chemical graphs. *Computational and structural biotechnology journal* **5**(6), 201302004 (2013)
 - [35] Xia, T., Ku, W.-S.: Geometric graph representation learning on protein structure prediction. In: *Proceedings of the 27th ACM SIGKDD Conference on Knowledge Discovery & Data Mining*, pp. 1873–1883 (2021)
 - [36] Morehead, A., Chen, X., Wu, T., Liu, J., Cheng, J.: Egr: Equivariant graph refinement and assessment of 3d protein complex structures. *arXiv preprint arXiv:2205.10390* (2022)
 - [37] Shlomi, J., Battaglia, P., Vlimant, J.-R.: Graph neural networks in particle physics. *Machine Learning: Science and Technology* **2**(2), 021001 (2020)
 - [38] Derrow-Pinion, A., She, J., Wong, D., Lange, O., Hester, T., Perez, L., Nunkesser, M., Lee, S., Guo, X., Wiltshire, B., *et al.*: Eta prediction with graph neural networks in google maps. In: *Proceedings of the 30th ACM International Conference on Information & Knowledge Management*, pp. 3767–3776 (2021)
 - [39] Ye, S., Liang, J., Liu, R., Zhu, X.: Symmetrical graph neural network for quantum chemistry with dual real and momenta space. *The Journal of Physical Chemistry A* **124**(34), 6945–6953 (2020)
 - [40] Han, J., Huang, W., Ma, H., Li, J., Tenenbaum, J.B., Gan, C.: Learning physical dynamics with subequivariant graph neural networks. *arXiv preprint arXiv:2210.06876* (2022)
 - [41] Morehead, A., Chen, C., Cheng, J.: Geometric transformers for protein interface contact prediction. In: *International Conference on Learning Representations* (2022). <https://openreview.net/forum?id=CS4463zx6Hi>
 - [42] Jumper, J., Evans, R., Pritzel, A., Green, T., Figurnov, M., Ronneberger, O.,

- Tunyasuvunakool, K., Bates, R., Židek, A., Potapenko, A., *et al.*: Highly accurate protein structure prediction with alphafold. *Nature* **596**(7873), 583–589 (2021)
- [43] Cohen, T., Welling, M.: Group equivariant convolutional networks. In: International Conference on Machine Learning, pp. 2990–2999 (2016). PMLR
- [44] Thomas, N., Smidt, T.E., Kearnes, S.M., Yang, L., Li, L., Kohlhoff, K., Riley, P.F.: Tensor field networks: Rotation- and translation-equivariant neural networks for 3d point clouds. *ArXiv abs/1802.08219* (2018)
- [45] Fuchs, F., Worrall, D., Fischer, V., Welling, M.: Se(3)-transformers: 3d roto-translation equivariant attention networks. *Advances in Neural Information Processing Systems* **33**, 1970–1981 (2020)
- [46] Jing, B., Eismann, S., Suriana, P., Townshend, R.J., Dror, R.: Learning from protein structure with geometric vector perceptrons. *arXiv preprint arXiv:2009.01411* (2020)
- [47] Jing, B., Eismann, S., Soni, P.N., Dror, R.O.: Equivariant graph neural networks for 3d macromolecular structure. *arXiv preprint arXiv:2106.03843* (2021)
- [48] Kofinas, M., Nagaraja, N., Gavves, E.: Roto-translated local coordinate frames for interacting dynamical systems. *Advances in Neural Information Processing Systems* **34**, 6417–6429 (2021)
- [49] Gasteiger, J., Becker, F., Günnemann, S.: Gemnet: Universal directional graph neural networks for molecules. *Advances in Neural Information Processing Systems* **34**, 6790–6802 (2021)
- [50] Schütt, K., Unke, O., Gastegger, M.: Equivariant message passing for the prediction of tensorial properties and molecular spectra. In: International Conference on Machine Learning, pp. 9377–9388 (2021). PMLR
- [51] Huang, W., Han, J., Rong, Y., Xu, T., Sun, F., Huang, J.: Equivariant graph mechanics networks with constraints. *arXiv preprint arXiv:2203.06442* (2022)
- [52] Thölke, P., De Fabritiis, G.: Equivariant transformers for neural network based molecular potentials. In: International Conference on Learning Representations (2022)
- [53] Du, W., Zhang, H., Du, Y., Meng, Q., Chen, W., Zheng, N., Shao, B., Liu, T.-Y.: SE(3) equivariant graph neural networks with complete local frames. In: Chaudhuri, K., Jegelka, S., Song, L., Szepesvari, C., Niu, G., Sabato, S. (eds.) *Proceedings of the 39th International Conference on Machine Learning. Proceedings of Machine Learning Research*, vol. 162, pp. 5583–5608. PMLR, ??? (2022). <https://proceedings.mlr.press/v162/du22e.html>

- [54] Aykent, S., Xia, T.: Gbpnet: Universal geometric representation learning on protein structures. In: Proceedings of the 28th ACM SIGKDD Conference on Knowledge Discovery and Data Mining. KDD '22, pp. 4–14. Association for Computing Machinery, New York, NY, USA (2022). <https://doi.org/10.1145/3534678.3539441> . <https://doi.org/10.1145/3534678.3539441>
- [55] Batzner, S., Musaelian, A., Sun, L., Geiger, M., Mailoa, J.P., Kornbluth, M., Molinari, N., Smidt, T.E., Kozinsky, B.: E (3)-equivariant graph neural networks for data-efficient and accurate interatomic potentials. *Nature communications* **13**(1), 2453 (2022)
- [56] Dangovski, R., Jing, L., Loh, C., Han, S., Srivastava, A., Cheung, B., Agrawal, P., Soljagic, M.: Equivariant self-supervised learning: Encouraging equivariance in representations. In: International Conference on Learning Representations (2021)
- [57] Xie, Y., Wen, J., Lau, K.W., Rehman, Y.A.U., Shen, J.: What should be equivariant in self-supervised learning. In: Proceedings of the IEEE/CVF Conference on Computer Vision and Pattern Recognition, pp. 4111–4120 (2022)
- [58] Adams, K., Pattanaik, L., Coley, C.W.: Learning 3d representations of molecular chirality with invariance to bond rotations. arXiv preprint arXiv:2110.04383 (2021)
- [59] Schneuing, A., Du, Y., Harris, C., Jamasb, A.R., Igashov, I., Du, Blundell, T.L., Lio, P., Gomes, C.P., Welling, M., Bronstein, M.M., Correia, B.: Structure-based Drug Design with Equivariant Diffusion Models (2023). <https://openreview.net/forum?id=uKmuzIuVl8z>
- [60] Townshend, R.J., Vögele, M., Suriana, P., Derry, A., Powers, A., Laloudakis, Y., Balachandar, S., Jing, B., Anderson, B., Eismann, S., et al.: Atom3d: Tasks on molecules in three dimensions. arXiv preprint arXiv:2012.04035 (2020)
- [61] Öztürk, H., Özgür, A., Ozkirimli, E.: Deepdta: deep drug–target binding affinity prediction. *Bioinformatics* **34**(17), 821–829 (2018)
- [62] Karimi, M., Wu, D., Wang, Z., Shen, Y.: Deepaffinity: interpretable deep learning of compound–protein affinity through unified recurrent and convolutional neural networks. *Bioinformatics* **35**(18), 3329–3338 (2019)
- [63] Bepler, T., Berger, B.: Learning protein sequence embeddings using information from structure. In: International Conference on Learning Representations (2019). <https://openreview.net/forum?id=SygLehCqtm>
- [64] Rao, R., Bhattacharya, N., Thomas, N., Duan, Y., Chen, P., Canny, J., Abbeel, P., Song, Y.: Evaluating protein transfer learning with tape. In: Wallach, H., Larochelle, H., Beygelzimer, A., Alché-Buc, F., Fox, E., Garnett,

- R. (eds.) Advances in Neural Information Processing Systems, vol. 32. Curran Associates, Inc., ??? (2019). <https://proceedings.neurips.cc/paper/2019/file/37f65c068b7723cd7809ee2d31d7861c-Paper.pdf>
- [65] Elnaggar, A., Heinzinger, M., Dallago, C., Rehawi, G., Wang, Y., Jones, L., Gibbs, T., Feher, T., Angerer, C., Steinegger, M., *et al.*: Prottrans: Toward understanding the language of life through self-supervised learning. *IEEE transactions on pattern analysis and machine intelligence* **44**(10), 7112–7127 (2021)
- [66] Nguyen, T., Le, H., Quinn, T.P., Nguyen, T., Le, T.D., Venkatesh, S.: Graphdta: Predicting drug–target binding affinity with graph neural networks. *Bioinformatics* **37**(8), 1140–1147 (2021)
- [67] Gainza, P., Sverrisson, F., Monti, F., Rodola, E., Boscaini, D., Bronstein, M., Correia, B.: Deciphering interaction fingerprints from protein molecular surfaces using geometric deep learning. *Nature Methods* **17**(2), 184–192 (2020)
- [68] Hermosilla, P., Schäfer, M., Lang, M., Fackelmann, G., Vázquez, P.-P., Kozlikova, B., Krone, M., Ritschel, T., Ropinski, T.: Intrinsic-extrinsic convolution and pooling for learning on 3d protein structures. In: International Conference on Learning Representations (2021). <https://openreview.net/forum?id=l0mSUROpwY>
- [69] Somnath, V.R., Bunne, C., Krause, A.: Multi-scale representation learning on proteins. In: Beygelzimer, A., Dauphin, Y., Liang, P., Vaughan, J.W. (eds.) Advances in Neural Information Processing Systems (2021). https://openreview.net/forum?id=-xEk43f_EO6
- [70] Wang, L., Liu, H., Liu, Y., Kurtin, J., Ji, S.: Learning hierarchical protein representations via complete 3d graph networks. In: The Eleventh International Conference on Learning Representations (2023). <https://openreview.net/forum?id=9X-hgLDLYkQ>
- [71] Liu, S., Guo, H., Tang, J.: Molecular geometry pretraining with SE(3)-invariant denoising distance matching. In: The Eleventh International Conference on Learning Representations (2023). <https://openreview.net/forum?id=CjTHVo1dvR>
- [72] Anderson, B., Hy, T.S., Kondor, R.: Cormorant: Covariant molecular neural networks. *Advances in neural information processing systems* **32** (2019)
- [73] Rezaei, M.A., Li, Y., Wu, D., Li, X., Li, C.: Deep learning in drug design: protein-ligand binding affinity prediction. *IEEE/ACM Transactions on Computational Biology and Bioinformatics* (2020)
- [74] Wang, R., Fang, X., Lu, Y., Yang, C.-Y., Wang, S.: The pdbind database: methodologies and updates. *Journal of medicinal chemistry* **48**(12), 4111–4119 (2005)

- [75] Uziela, K., Menéndez Hurtado, D., Shu, N., Wallner, B., Elofsson, A.: Proq3d: improved model quality assessments using deep learning. *Bioinformatics* **33**(10), 1578–1580 (2017)
- [76] Olechnovič, K., Venclovas, Č.: Voromqa: Assessment of protein structure quality using interatomic contact areas. *Proteins: Structure, Function, and Bioinformatics* **85**(6), 1131–1145 (2017)
- [77] Zhang, J., Zhang, Y.: A novel side-chain orientation dependent potential derived from random-walk reference state for protein fold selection and structure prediction. *PloS one* **5**(10), 15386 (2010)
- [78] Karasikov, M., Pagès, G., Grudin, S.: Smooth orientation-dependent scoring function for coarse-grained protein quality assessment. *Bioinformatics* **35**(16), 2801–2808 (2019)
- [79] Pagès, G., Charmettant, B., Grudin, S.: Protein model quality assessment using 3d oriented convolutional neural networks. *Bioinformatics* **35**(18), 3313–3319 (2019)
- [80] Klicpera, J., Groß, J., Günnemann, S.: Directional message passing for molecular graphs. *arXiv preprint arXiv:2003.03123* (2020)
- [81] Baldassarre, F., Menéndez Hurtado, D., Elofsson, A., Azizpour, H.: Graphqa: protein model quality assessment using graph convolutional networks. *Bioinformatics* **37**(3), 360–366 (2021)
- [82] Zemla, A.: Lga: a method for finding 3d similarities in protein structures. *Nucleic acids research* **31**(13), 3370–3374 (2003)
- [83] Kryshchak, A., Schwede, T., Topf, M., Fidelis, K., Moult, J.: Critical assessment of methods of protein structure prediction (casp)—round xiv. *Proteins: Structure, Function, and Bioinformatics* **89**(12), 1607–1617 (2021)
- [84] Dieng, A.B., Kim, Y., Rush, A.M., Blei, D.M.: Avoiding latent variable collapse with generative skip models. In: Chaudhuri, K., Sugiyama, M. (eds.) *Proceedings of the Twenty-Second International Conference on Artificial Intelligence and Statistics. Proceedings of Machine Learning Research*, vol. 89, pp. 2397–2405. PMLR, ??? (2019). <https://proceedings.mlr.press/v89/dieng19a.html>
- [85] Wang, L., Liu, Y., Lin, Y., Liu, H., Ji, S.: ComENet: Towards complete and efficient message passing for 3d molecular graphs. In: Oh, A.H., Agarwal, A., Belgrave, D., Cho, K. (eds.) *Advances in Neural Information Processing Systems* (2022). <https://openreview.net/forum?id=mCzMqeWSFJ>
- [86] Brandstetter, J., Hesselink, R., Pol, E., Bekkers, E.J., Welling, M.: Geometric and physical quantities improve e(3) equivariant message passing. *arXiv preprint*

arXiv:2110.02905 (2021)

- [87] Du, W., Du, Y., Wang, L., Feng, D., Wang, G., Ji, S., Gomes, C., Ma, Z.-M.: A new perspective on building efficient and expressive 3d equivariant graph neural networks. arXiv preprint arXiv:2304.04757 (2023)
- [88] Zaheer, M., Kottur, S., Ravanbakhsh, S., Póczos, B., Salakhutdinov, R.R., Smola, A.J.: Deep sets. *Advances in neural information processing systems* **30** (2017)
- [89] Qiao, Z., Nie, W., Vahdat, A., Miller III, T.F., Anandkumar, A.: Dynamic-backbone protein-ligand structure prediction with multiscale generative diffusion models. arXiv preprint arXiv:2209.15171 (2022)
- [90] Ingraham, J., Garg, V., Barzilay, R., Jaakkola, T.: Generative models for graph-based protein design. *Advances in neural information processing systems* **32** (2019)
- [91] Kuhlman, B., Baker, D.: Native protein sequences are close to optimal for their structures. *Proceedings of the National Academy of Sciences* **97**(19), 10383–10388 (2000)
- [92] Gao, Z., Tan, C., Li, S.Z.: Pifold: Toward effective and efficient protein inverse folding. arXiv preprint arXiv:2209.12643 (2022)
- [93] Van Rossum, G., Drake, F.L.: *Python 3 Reference Manual*. CreateSpace, Scotts Valley, CA (2009)
- [94] Paszke, A., Gross, S., Massa, F., Lerer, A., Bradbury, J., Chanan, G., Killeen, T., Lin, Z., Gimeshin, N., Antiga, L., Desmaison, A., Kopf, A., Yang, E., DeVito, Z., Raison, M., Tejani, A., Chilamkurthy, S., Steiner, B., Fang, L., Bai, J., Chintala, S.: Pytorch: An imperative style, high-performance deep learning library. In: Wallach, H., Larochelle, H., Beygelzimer, A., Alché-Buc, F., Fox, E., Garnett, R. (eds.) *Advances in Neural Information Processing Systems 32*, pp. 8024–8035. Curran Associates, Inc., ??? (2019)
- [95] Falcon, e.a. WA: Pytorch lightning. <https://github.com/PyTorchLightning/pytorch-lightning> **3** (2019)
- [96] Fey, M., Lenssen, J.E.: Fast graph representation learning with pytorch geometric. ArXiv **abs/1903.02428** (2019)

Appendix A Proofs.

A.1 Proof of Proposition 1.

Proof. Suppose the vector-valued features given to the corresponding **GCPConv** layers in GCPNET are node features χ_i and edge features ξ_{ij} that are $O(3)$ -equivariant (i.e., 3D rotation and reflection-equivariant) by way of their construction. Additionally, suppose the scalar-valued features given to the respective **GCPConv** layers in GCPNET are $E(3)$ -invariant (i.e., 3D rotation, reflection, and translation-invariant) node features h_i and edge features e_{ij} .

Translation equivariance. In line with [53], the **Centralize** operation on Line 2 of Algorithm 1 first ensures that \mathbf{X}^0 becomes 3D translation invariant by the following procedure. Let $\mathbf{X}(t) = (\mathbf{x}_1(t), \dots, \mathbf{x}_n(t))$ represent a many-body system at time t , where the centroid of the system is defined as

$$C(t) = \frac{\mathbf{x}_1(t) + \dots + \mathbf{x}_n(t)}{n}. \quad (\text{A1})$$

Note that in uniformly translating the position of the system by a vector \mathbf{v} , we have $\mathbf{X}(t) + \mathbf{v} \rightarrow C(t) + \mathbf{v}$, meaning that the centroid of the system translates in the same manner as the system itself. However, note that if at time $t = 0$ we recenter the origin of \mathbf{X} to its centroid, we have

$$\mathbf{X}(t) - C(0) \xrightarrow{\text{translation by } \mathbf{v} \text{ at } t=0} \mathbf{X}(t) - C(0)$$

which implies the system \mathbf{X} is translation-invariant under the centralized reference $\mathbf{X}(t) - C(0)$ when the translation vector \mathbf{v} is applied to \mathbf{X} at time $t = 0$. Concretely, in the case of translation-invariant tasks such as predicting molecular properties or classifying point clouds, here we have successfully achieved 3D translation invariance. Moreover, for translation-equivariant tasks such as forecasting the positions of a many-body system, we can achieve translation equivariance by simply adding $C(0)$ back to the predicted positions. Therefore, using the above methodology, GCPNETS are translation equivariant.

Permutation equivariance. Succinctly, we note that since GCPNET operates on graph-structured input data, permutation equivariance is guaranteed by design. For further discussion of why our proposed method as well as why other graph-based algorithms proposed previously are inherently permutation-equivariant, we refer readers to [88]. Therefore, GCPNETS are permutation-equivariant.

SO(3)-equivariant frames. On Line 3 of Algorithm 1, the **Localize** operation constructs $SO(3)$ -equivariant (i.e., 3D rotation-equivariant) frames \mathcal{F}_{ij} in the following manner.

Define our frame encodings as

$$\mathcal{F}_{ij}^t = (a_{ij}^t, b_{ij}^t, c_{ij}^t), \quad (\text{A2})$$

where we have

$$a_{ij}^t = \frac{x_i^t - x_j^t}{\|x_i^t - x_j^t\|}, b_{ij}^t = \frac{x_i^t \times x_j^t}{\|x_i^t \times x_j^t\|}, c_{ij}^t = a_{ij}^t \times b_{ij}^t. \quad (\text{A3})$$

The proof that \mathcal{F}_{ij}^t is equivariant under $\text{SO}(3)$ transformations of its input space is included in [53]. However, for completeness, we include a version of it here.

Let $g \in \text{SO}(3)$ be an action under which the positions in X transform equivariantly, and \mathcal{F}_{ij}^t be defined as we have it in Equation A2 above. That is, we have

$$(\mathbf{x}_1(t), \dots, \mathbf{x}_n(t)) \xrightarrow{g} (g\mathbf{x}_1(t), \dots, g\mathbf{x}_n(t)),$$

where from the definition of a_{ij}^t in Equation A3 we have

$$a_{ij}^t \xrightarrow{g} ga_{ij}^t.$$

Considering b_{ij}^t , from Equation A3 we have

$$\begin{aligned} (gx_i(t)) \times (gx_j(t)) &= \det(g)(g^T)^{-1}(x_i(t) \times x_j(t)) \\ &= g(x_i(t) \times x_j(t)), \end{aligned} \quad (\text{A4})$$

where using $g^{-1} = g^T$ for the orthogonal matrix g gives us Equation A4. Consequently, $b_{ij}^t \xrightarrow{g} gb_{ij}^t$. Lastly, by applying Equation A4 once again, we have that $c_{ij}^t \xrightarrow{g} gc_{ij}^t$.

Moreover, note that under reflections of x , we have $R : x \rightarrow -x$ which gives us $a_{ij}^t \rightarrow -a_{ij}^t$. Thereafter, by the right-hand rule, the cross product of two equivariant vectors gives us a pseudo-vector $b_{ij}^t = x_i^t \times x_j^t \rightarrow b_{ij}^t$, where subsequently it is implied that $c_{ij}^t \rightarrow -c_{ij}^t$. Consequently, we have $\det(-a_{ij}^t, b_{ij}^t, -c_{ij}^t) = 1$, informing us that the frame encodings \mathcal{F}_{ij}^t are not reflection-equivariant (a symmetry that is important to not enforce when learning representations of chiral molecules such as proteins). Therefore, the frame encodings within GCPNET are $\text{SO}(3)$ -equivariant.

Note, after the construction of these frames, that they are used on Line 4 of Algorithm 1 to embed all node and edge features (i.e., h_i , e_{ij} , χ_i , and ξ_{ij}) using a single **GCP** module as well as in all subsequent **GCP** modules. We will now prove that the feature updates each **GCP** module makes with the frame encodings \mathcal{F}_{ij}^t defined in Equation A2 are $\text{SO}(3)$ -equivariant.

SO(3)-equivariant GCP module. The operations of a **GCP** module are illustrated in Figure 3 and derived in Section 3.2.1. Their $\text{SO}(3)$ invariance for scalar feature updates and $\text{SO}(3)$ equivariance for vector-valued feature updates is proven as follows.

Following the proof of $\text{O}(3)$ equivariance for the GVP module in [46], the proof of $\text{SO}(3)$ equivariance within the **GCP** module is similar, with the following modifications. Within the **GCP** module, the vector-valued features (processed separately for nodes and edges) are fed not only through a bottleneck block comprised of downward and upward projection matrices \mathbf{D}_z and \mathbf{U}_z but are also fed into a dedicated

downward projection matrix \mathbf{D}_S . The output of matrix multiplication between $O(3)$ -equivariant vector features and \mathbf{D}_S yields $O(3)$ -equivariant vector features v_{i_S} that are used as unique inputs for an $SO(3)$ -invariant scalarization operation. In particular, the following demonstrates the invariance of our design for matrix multiplication with our **GCP** module’s projection matrices (e.g., \mathbf{D}_S). Suppose $\mathbf{W}_h \in \mathbb{R}^{h \times v}$, $\mathbf{V} \in \mathbb{R}^{v \times 3}$, and $\mathbf{Q} \in SO(3) \in \mathbb{R}^{3 \times 3}$. In line with [46], observe for $\mathbf{D} = (\mathbf{Q}\mathbf{V}^T) \in \mathbb{R}^{3 \times v}$ that

$$\|\mathbf{W}_h \mathbf{D}^T\|_2 = \|\mathbf{W}_h (\mathbf{V}^T)^T\|_2 = \|\mathbf{W}_h \mathbf{V}\|_2.$$

Specifically, our $SO(3)$ -invariant scalarization operation is defined as

$$q_{ij} = (v_{i_S} \cdot a_{ij}^t, v_{i_S} \cdot b_{ij}^t, v_{i_S} \cdot c_{ij}^t), \quad (\text{A5})$$

where $\mathcal{F}_{ij}^t = (a_{ij}^t, b_{ij}^t, c_{ij}^t)$ denotes the $SO(3)$ -equivariant frame encodings defined in Equations A2 and A3.

To prove that Equation A5 yields $SO(3)$ -invariant scalar features, let $g \in SO(3)$ be an arbitrary orthogonal transformation. Then we have $v_{i_S} \rightarrow gv_{i_S}$, and similarly $\mathcal{F}_{ij}^t = (a_{ij}^t, b_{ij}^t, c_{ij}^t) \rightarrow (ga_{ij}^t, gb_{ij}^t, gc_{ij}^t)$. Now, similar to [53], we can derive that Equation A5 becomes

$$\begin{aligned} & (v_{i_S} \cdot a_{ij}^t, v_{i_S} \cdot b_{ij}^t, v_{i_S} \cdot c_{ij}^t) \\ & \rightarrow ((v_{i_S})^T g^T ga_{ij}^t, (v_{i_S})^T g^T gb_{ij}^t, (v_{i_S})^T g^T gc_{ij}^t) \\ & = (v_{i_S} \cdot a_{ij}^t, v_{i_S} \cdot b_{ij}^t, v_{i_S} \cdot c_{ij}^t), \end{aligned} \quad (\text{A6})$$

where we used the fact that $g^T g = I$ due to the orthogonality of g (with I being the identity matrix). Therefore, the scalarization operation proposed in Equation A5, and previously in Equation 3 (in an alternative form), yields $SO(3)$ -invariant scalars, which is in line with the results of [89].

The output of Equation A5, q_{ij} , is then aggregated in Equation 4 and concatenated in Equation 5 with the **GCP** module’s remaining $O(3)$ -invariant scalar features (i.e., L_2 vector norm features). Note that introducing $SO(3)$ -invariant scalar information into the **GCP** module in this way breaks the 3D reflection symmetry that previous geometric graph convolution modules enforced [46], now giving rise within the **GCP** module to $SO(3)$ -invariant and $SO(3)$ -equivariant updates to scalar and vector-valued features, respectively. Therefore, scalar and vector-valued feature updates for nodes and edges within the **GCP** module are $SO(3)$ -invariant and $SO(3)$ -equivariant, respectively.

As in Section 3.3.1, we now turn to discuss the operations within a single **GCPCConv** layer, in particular proving that they maintain the respective $SO(3)$ invariance and $SO(3)$ equivariance for scalar and vector-valued features that the **GCP** module provides.

$SO(3)$ -equivariant GCPCConv layer. Via the corresponding proof in [46], by way of induction all such operations in Equations 10-15 are respectively $SE(3)$ -invariant and $SO(3)$ -equivariant for features $m_{ij}^l = (m_{e_{ij}}^l, m_{\xi_{ij}}^l)$. Thereby, so are features $n_i^l = (h_i^l, \chi_i^l)$, given that the proof of equivariance for the equivariant

LayerNorm and **Dropout** operations employed within each **GCPConv** has previously been concretized by [46]. Equation 17 concludes the operations of a single **GCPConv** layer by, as desired, updating the positions of each node i in the 3D input graph. To do so, **GCPConv** residually updates current node positions x_i^{l-1} using $\text{SO}(3)$ -equivariant vector-valued features $\chi_{p_i}^l$. Therefore, **GCPConv** layers are $\text{SO}(3)$ -invariant for scalar feature updates and $\text{SO}(3)$ -equivariant for vector-valued node position and feature updates.

SE(3)-equivariant GCPNet. Lastly, as desired, Line 10 of Algorithm 1 adds $C(0)$ back to the predicted node positions \mathbf{X}^l as provided by each **GCPConv** layer, ultimately imbuing position updates within \mathbf{X}^l with $\text{SE}(3)$ equivariance. Line 14 then concludes GCPNET by using the latest frame encodings \mathcal{F}_{ij}^t to perform, as desired, a final $\text{SO}(3)$ -invariant and $\text{SO}(3)$ -equivariant projection for scalar and vector-valued features, respectively. Therefore, as desired, GCPNETS are $\text{SE}(3)$ -invariant for scalar feature updates, $\text{SE}(3)$ -equivariant for vector-valued node position and feature updates, and, as a consequence, satisfy the constraint proposed in Def. 1. \square

A.2 Proof of Proposition 2.

Proof. The proof of $\text{SE}(3)$ invariance for scalar node and edge features, h_i and e_{ij} , follows as a corollary of Appendix A.1 (**SE(3)-equivariant GCPNet**). Therefore, GCPNETS are $\text{SE}(3)$ -invariant concerning their predicted scalar node and edge features and, as a consequence, are geometrically self-consistent according to the constraint in Def. 2. \square

A.3 Proof of Proposition 3.

Proof. Suppose that GCPNET designates its local geometric representation for layer t to be $\mathcal{F}_{ij}^t = (a_{ij}^t, b_{ij}^t, c_{ij}^t)$, where $a_{ij}^t = \frac{x_i^t - x_j^t}{\|x_i^t - x_j^t\|}$, $b_{ij}^t = \frac{x_i^t \times x_j^t}{\|x_i^t \times x_j^t\|}$, and $c_{ij}^t = a_{ij}^t \times b_{ij}^t$, respectively. As in [53], this formulation of \mathcal{F}_{ij}^t is proven in Appendix A.1 (*SO(3)-equivariant frames*) to be an $\text{SO}(3)$ -equivariant local orthonormal basis at the tangent space of x_i^t and is thereby geometrically complete. Note this implies that GCPNET permits no loss of geometric information as discussed in Appendix A.5 of [53]. Therefore, GCPNETS are geometry-complete and satisfy the constraint proposed in Def. 3. \square

Appendix B Additional Experiments and Results.

In this section, we explore an additional modeling task, computational protein design, with its implementation details being discussed in Appendix C.

CPD, Node Classification. Computational protein design (CPD) investigates a method’s ability to design native-like protein sequences. In our CPD experiments, we explore fixed-backbone sequence design, where methods are provided with the 3D backbone structure of a protein and asked to generate a corresponding sequence. We train and evaluate each CPD method on the CATH 4.2 dataset created by [90]. This dataset contains 18,204, 608, and 1,120 training, validation, and test proteins, respectively, where all available protein structures with 40% nonredundancy are partitioned by their CATH (class, architecture, topology/fold, homologous superfamily) classification. Baseline comparison methods for this task include a mixture of state-of-the-art Transformers, GNNs, and ENNs.

Under the assumption that native sequences are optimized for their structures [91], the metrics with which we evaluate each method measure how well a method can distinguish a native-like sequence from a non-native sequence. In particular, following [90], we adopt model perplexity as a measure of how well a method can model the language of native protein sequences. Similarly, we employ native sequence recovery (i.e., amino acid recovery) rates as a way of evaluating, on average, how well each method can design sequences that resemble native protein sequences.

Table B1: Comparison of GCPNET with baseline methods for the CPD task. Results are reported in terms of the perplexity and amino acid recovery rates of each method for fixed-backbone sequence design. The best results for this task are in **bold**, and the second-best results are underlined.

Method	Perplexity ↓			Recovery ↑		
	Short	Single	All	Short	Single	All
STran* [2019]	8.54	9.03	6.85	28.30	27.60	36.40
SGNN* [2020]	8.31	8.88	6.55	28.40	28.10	37.30
GVP* [2021]	<u>7.10</u>	<u>7.44</u>	<u>5.29</u>	32.10	32.00	40.20
GBP* [2022]	6.14	6.46	5.03	33.22	33.22	42.70
GCPNET w/o Frames	7.71	8.18	5.87	31.82	31.72	<u>41.18</u>
GCPNET w/o RESGCP	9.63	9.88	7.09	27.27	27.02	35.27
GCPNET w/o Scalars	18.51	18.37	18.17	8.70	8.55	8.62
GCPNET w/o Vectors	10.41	10.53	8.87	26.42	26.23	28.99
GCPNET	8.22	8.60	6.06	33.33	<u>32.86</u>	40.32

Table B1 shows that, in representing proteins as amino acid residue-level graphs, GCPNET matches or exceeds the performance of several state-of-the-art prediction methods for CPD. In particular, GCPNET improves upon state-of-the-art short sequence recovery rates of previous methods by 0.5% on average while maintaining competitive performance against other methods in all other metrics. We note that

all CPD methods marked with * perform model inference autoregressively, introducing a significant computational bottleneck for real-world applications of these models. Inference with GCPNET, in contrast, is designed for direct prediction of amino acid sequences corresponding to a 3D protein structure, thereby decreasing inference runtime by more than a factor of two compared to other methods. While being a simple direct-shot prediction method for CPD, GCPNET is still able to achieve competitive results in terms of amino acid recovery rates for sequence generation, with reasonable results in terms of perplexity as well.

Interestingly, in the context of CPD, an ablation of our equivariant local frames \mathcal{F}_{ij} reveals that such frames are not useful for increasing GCPNET’s confidence in its structural understanding of the language of proteins (i.e., its perplexity). This suggests that future work could involve exploring alternative geometric encoding schemes for residue-based graphs when approaching the CPD task [92] with GCPNET. This finding highlights the fact that the local frames \mathcal{F}_{ij} appear to be most useful in the context of representation learning on atomic graphs where lower-level molecular motifs are likely to appear, implying that future work towards improving CPD results with GCPNET could involve developing novel atom-level encoding schemes for residue-based graph predictions to leverage the promising results GCPNET yields in other dataset contexts. Nonetheless, our remaining ablations demonstrate that other design characteristics of GCPNET such as the **ResGCP** module and scalar and vector-valued feature representations enable GCPNET to better decode sequence-based information from 3D protein structures.

Table B2: Summary of GCPNET’s node and edge features for 3D input graphs derived for the LBA and PSR tasks. Here, N and E denote the number of nodes and edges in \mathcal{G} , respectively.

	Feature	Type	Shape
Node Features (h)	One-hot encoding of atom type	Categorical (Scalar)	$N \times 9$
Node Features (χ)	Directional encoding of orientation	Numeric (Vector)	$N \times 2$
Edge Features (e)	Radial basis distance embedding	Numeric (Scalar)	$E \times 16$
Edge Features (ξ)	Pairwise atom position displacement	Numeric (Vector)	$E \times 1$
Total	Node features		$N \times 11$
	Edge features		$E \times 17$

Appendix C Implementation Details.

Featurization. As shown in Table B2, for the LBA and PSR tasks, in each 3D input graph, we include as a scalar node feature an atom’s type using a 9-dimensional one-hot encoding vector for each atom. As vector-valued node features, we include *forward* and *reverse* unit vectors in the direction of $x_{i+1} - x_i$ and $x_{i-1} - x_i$, respectively (i.e., the node’s 3D orientation). For the input 3D graphs’ scalar edge features, we encode the distance $\|x_i - x_j\|_2$ using Gaussian radial basis functions, where we use 16 radial basis functions with centers evenly distributed between 0 and 20 units (e.g., Angstrom). For

Table B3: Summary of GCPNET’s node and edge features for 3D input graphs derived for the CPD task.

	Feature	Type	Shape
Node Features (h)	Dihedral angle encoding	Numeric (Scalar)	$N \times 6$
Node Features (χ)	Orientation and sidechain encoding	Numeric (Vector)	$N \times 3$
Edge Features (e)	Distance and positional embedding	Numeric (Scalar)	$E \times 32$
Edge Features (ξ)	Pairwise atom position displacement	Numeric (Vector)	$E \times 1$
Total	Node features		$N \times 9$
	Edge features		$E \times 33$

Table B4: Summary of GCPNET’s node and edge features for 3D input graphs derived for the NMS task.

	Feature	Type	Shape
Node Features (h)	Invariant velocity encoding	Numeric (Scalar)	$N \times 1$
Node Features (χ)	Velocity and orientation encoding	Numeric (Vector)	$N \times 3$
Edge Features (e)	Edge and distance embedding	Numeric (Scalar)	$E \times 17$
Edge Features (ξ)	Pairwise atom position displacement	Numeric (Vector)	$E \times 1$
Total	Node features		$N \times 4$
	Edge features		$E \times 18$

the graphs’ vector-valued edge features, we encode the unit vector in the direction of $x_i - x_j$ (i.e., pairwise atom position displacements).

As displayed in Table B3, for the CPD task, in each 3D input graph, we include as scalar node features an encoding of each amino acid residue’s dihedral angles $\{\sin, \cos\} \circ \{\phi, \psi, \omega\}$, where Φ , ψ , and ω are the dihedral angles computed from the corresponding protein’s C_{i-1} , N_i , C_i , and N_{i+1} backbone atoms. We then include as vector-valued node features each node’s 3D orientation. For edge features, we use Gaussian radial basis function distance encodings as scalar edge features and pairwise atom position displacements as vector-valued edge features.

As illustrated in Table B4, for the NMS task, in each 3D input graph, we include as a scalar node feature an invariant encoding of each node’s velocity vector, namely $\sqrt{v_i^2}$. Each node’s velocity and orientation are encoded as vector-valued node features. Scalar edge features are represented as Gaussian radial basis distance encodings as well as the product of the charges in each node pair (i.e., $c_i c_j$). Lastly, vector-valued edge features are represented as pairwise atom position displacements.

Hardware Used. The Oak Ridge Leadership Facility (OLCF) at the Oak Ridge National Laboratory (ORNL) is an open science computing facility that supports HPC research. The OLCF houses the Summit compute cluster. Summit, launched in 2018, delivers 8 times the computational performance of Titan’s 18,688 nodes, using only 4,608 nodes. Like Titan, Summit has a hybrid architecture, and each node contains multiple IBM POWER9 CPUs and NVIDIA Volta GPUs all connected with NVIDIA’s high-speed NVLink. Each node has over half a terabyte of coherent memory (high

bandwidth memory + DDR4) addressable by all CPUs and GPUs plus 800GB of non-volatile RAM that can be used as a burst buffer or as extended memory. To provide a high rate of I/O throughput, the nodes are connected in a non-blocking fat-tree using a dual-rail Mellanox EDR InfiniBand interconnect. We used the Summit compute cluster to train all our models. For the LBA and NMS tasks, we used 16GB NVIDIA Tesla V100 GPUs for model training, whereas for the memory-intensive PSR and CPD tasks, we used 32GB V100 GPUs instead.

Software Used. We used Python 3.8.12 [93], PyTorch 1.10.2 [94], PyTorch Lightning 1.7.7 [95], and PyTorch Geometric 2.1.0post0 [96] to run our deep learning experiments. For each model trained, PyTorch Lightning was used to facilitate model checkpointing, metrics reporting, and distributed data parallelism across 6 V100 GPUs. A more in-depth description of the software environment used to train and run inference with our models is available at <https://github.com/BioinfoMachineLearning/GCPNet>.

Hyperparameters. As shown in Tables C5, C6, C7, and C8, we use a learning rate of 10^{-4} for all GCPNET models. The learning rate is kept constant throughout each model’s training. For the NMS task, each model is trained for a minimum of 100 epochs and a maximum of 12,000 epochs. For all other tasks, each model is trained for a minimum of 100 epochs and a maximum of 1,000 epochs. For a given task, models with the best loss on the corresponding validation data split are then tested on the test split for the respective task. Note that, for the RS task, we do not perform any model hyperparameter tuning, following previous conventions from [59].

Table C5: Hyperparameter search space for all GCPNET models through which we searched to obtain strong performance on the LBA task’s validation split. The final parameters for the standard GCPNET model for the LBA task are in **bold**.

Hyperparameter	Search Space
Number of GCPNET Layers	7, 8
Number of GCP Message-Passing Layers	8
χ Hidden Dimensionality	16 , 32
Learning Rate	0.0001 , 0.0003
Weight Decay Rate	0
GCP Dropout Rate	0.1 , 0.25
Dense Layer Dropout Rate	0.1 , 0.25

Table C6: Hyperparameter search space for all GCPNET models through which we searched to obtain strong performance on the PSR task’s validation split. The final parameters for the standard GCPNET model for the PSR task are in **bold**.

Hyperparameter	Search Space
Number of GCPNET Layers	5
Number of GCP Message-Passing Layers	8
χ Hidden Dimensionality	16 , 32
Learning Rate	0.0001 , 0.0003
Weight Decay Rate	0 , 0.0001
GCP Dropout Rate	0.1 , 0.25
Dense Layer Dropout Rate	0.1 , 0.25

Table C7: Hyperparameter search space for all GCPNET models through which we searched to obtain strong performance on the CPD task’s validation split. The final parameters for the standard GCPNET model for the CPD task are in **bold**.

Hyperparameter	Search Space
Number of GCPNET Encoder Layers	9
Number of GCPNET Decoder Layers	3
Number of GCP Message-Passing Layers	8
χ Hidden Dimensionality	16 , 32
Learning Rate	0.0001
Weight Decay Rate	0.0, 10^{-8} , 0.0001
GCP Dropout Rate	0.1, 0.2 , 0.25, 0.4
Decoder Residual Updates	False, True

Table C8: Hyperparameter search space for all GCPNET models through which we searched to obtain strong performance on the NMS task’s validation split. The final parameters for the standard GCPNET model for the NMS task are in **bold**.

Hyperparameter	Search Space
Number of GCPNET Layers	4 , 7
Number of GCP Message-Passing Layers	8
χ Hidden Dimensionality	16
Learning Rate	0.0001 , 0.0003
Weight Decay Rate	0
GCP Dropout Rate	0.0, 0.1